Spatio-temporal variability of flooded areas in the Ouémé floodplain (Benin, West Africa) from 2015 to 2023

Noémie Ferdinand, Alexis Chaigneau, Alexei Kouraev, Yves Morel, Olaègbè Victor Okpeitcha, Sylvain Biancamaria, Sylvain Ferrant

Spatio-temporal variability of flooded areas in the Ouémé floodplain (Benin, West Africa) from 2015 to 2023.

Noémie Ferdinand[a,*], Alexis Chaigneau[a,b], Alexei Kouraev[a], Yves Morel[a,g], Olaègbè Victor Okpeitcha[c,d,e], Sylvain Biancamaria[a], Sylvain Ferrant[f]

[a] Laboratoire d'Etudes en Géophysique et Océanographie Spatial (LEGOS), Université de Toulouse, CNES, CNRS, IRD, UPS, Toulouse, France.

[b] Department of Water – Environment – Oceanography, University of Science and Technology of Hanoi (USTH), Vietnam Academy of Science and Technology (VAST), Hanoi, Vietnam

[c] PRODATA SARL, Cotonou, Bénin.

[d] Institut de Recherches Halieutiques et Océanologiques du Bénin (IRHOB), Cotonou, Bénin.

[e] International Chair in Mathematical Physics and Applications (ICMPA–UNESCO Chair), University of Abomey-Calavi, Cotonou, Benin

[f] Centre d'Etudes Spatiales de la Biosphère (CESBIO), Université de Toulouse, CNES/CNRS/INRAE/IRD/UT3, Toulouse, France

[g] Laboratoire d'Océanographie Physique et Spatiale (LOPS), University of Brest, CNRS/IRD/ Ifremer/IUEM, Brest, France

***Corresponding author:** Noémie FERDINAND, noemie.ferdinand@utoulouse.fr

Abstract

Study region

Ouémé floodplain, southern Benin, West Africa.

Study focus

The Ouémé floodplain is a vast hydrological system feeding the Nokoué lagoon via the Sô and Ouémé rivers, crossing an extensive wetland region. Driven by the African monsoon, this area is marked by pronounced seasonal and interannual hydrological variability, leading to recurrent flooding that significantly threatens local communities' safety and livelihoods. This study aims to assess the spatio-temporal variability of flooded areas in the Ouémé floodplain from 2015 to 2023, using both in-situ measurements and satellite remote sensing.

New hydrological insights for the region

The analysis reveals a clear seasonal cycle of flooding, modulated by interannual variability. Sentinel-1A water/land masks show that flood extent fluctuates widely, ranging from 20 to 160 km², and identify the Sô region as the most flood-prone area. Importantly, the study detects a significant upward trend in flood extent over the study period. Flood dynamics are primarily governed by cumulative January–September rainfall, with a critical threshold of 1070 mm beyond which inundation expands rapidly. River altimetry data further indicate a water surface elevation threshold of 6 m in the Ouémé river, above which flood expansion intensifies. The analysis highlights the emergence of temporary hydrological connections during flood events, adding complexity to floodplain hydrodynamics and enhancing connectivity across the basin. Overall, this study provides new insights into the mechanisms driving floods in the Ouémé floodplain using remote sensing.

Keywords Flood; floodplain; synthetic aperture radar; remote sensing; West Africa

1. Introduction

Floodplains are critical ecosystems that support both biodiversity and human livelihoods, particularly through agriculture, due to their fertile soils and abundant natural resources. Defined by Junk et al. (1990) as "areas of low-lying land that are subject to inundation by lateral overflow water from rivers or lakes with which they are associated," floodplains serve as essential zones for food production and economic activity. However, communities inhabiting these regions face dual challenges: while they benefit from the ecosystem services, they are also highly vulnerable to flooding.

Globally, floods represent the most frequent natural disaster, accounting for approximately 45% of all recorded events (Wallemacq et al., 2018), and affecting 1.8 billion people, which represent 23% of the global population (Rentschler et al., 2022). This vulnerability is compounded by growing population pressure in flood-prone zones. While floods are often triggered by extreme weather events—such as intense rainfall and river overflow—their severity is increasingly influenced by human-induced factors, including urbanization, land-use change, and infrastructure development (Wang et al., 2022), which disrupt natural hydrological dynamics.

In West Africa, the frequency and intensity of extreme weather events have intensified significantly in recent decades, impacting over 600,000 people across 16 countries (Di Baldassarre et al., 2010). Between 1950 and 2019, floods claimed an estimated 27,000 lives across Africa (Tramblay et al., 2020), a number expected to rise due to climate change-driven increases in precipitation intensity (Dore et al., 2005).

The Ouémé floodplain, located in southern Benin (West Africa), is formed by the Sô and Ouémé rivers that feed the Nokoué lagoon in freshwater (see Fig. 1). This region is influenced by the West African monsoon, driven by the seasonal migration of the Intertropical Convergence Zone (ITCZ) (Sultan et al., 2003). Due to intense rainfall and flat topography, the

Ouémé floodplain experiences annual flooding between August and November (Conway et al., 2004). Natural variability in the intensity of the West African monsoon results in interannual variations in the extent and impacts of flooding.

In recent years, the 2010 flood was particularly devastating, resulting in 46 deaths. In total, 680,000 people across 55 villages were affected, with 150,000 persons moved away. The flood also damaged more than 55,000 houses, 450 schools, and 90 medical centres and triggered outbreaks of waterborne diseases such as cholera, malaria, and diarrheal infections. Economic losses were estimated at 160 million USD with nearly 200,000 hectares of agricultural land devasted and 80,000 livestock lost (*Post-catastrophic need assessment report*, 2011; Ahouanga et al., 2014). Since 2010, large-scale floods have continued to occur regularly, though with less severe consequences.

Given the social, economic, and environmental impacts of flooding, understanding the dynamics of the Ouémé floodplain complex hydrological system is essential to anticipate and mitigate future risks. Hydrological flows in this region are largely influenced by wetlands and flood-prone zones, making it crucial to characterize these areas and their seasonal variability.

Recent advancements in flood risk assessment within the Ouémé catchment have increasingly employed Geographic Information Systems (GIS) and multi-criteria analysis to enhance the spatial identification of flood-prone areas. These approaches integrate hydro-geological parameters, socio-economic vulnerability, and exposure indicators to generate comprehensive flood risk maps. Notably, recent studies focusing on the Ouémé floodplain have revealed that approximately 21.5% of the lower valley is exposed to high and very high flood risk, with the southern regions being the most affected (Bossa et al., 2024). However, a significant gap remains in the literature, as most prior studies on the Ouémé catchment have primarily addressed flood events occurring north of Bonou, without considering the distinct dynamics of the downstream floodplain (Hounkpè et al., 2015; Amoussou et al., 2022; Quenum et al., 2022).

Various studies have explored flood detection using satellite data. One approach relies on optical sensors due to their high data availability and suitable spatial and temporal resolutions. Several optical sensors with different spatio-temporal resolution, such as MODIS, Suomi-NPP-VIIRS, Sentinel-2 and Landsat-8 have been used in flood detection research (Brakenridge et al. 2006; Ji et al. 2015; Du et al. 2016; Li et al. 2018). However, a key limitation of optical sensors is their susceptibility to cloud cover, which obstructs data acquisition.

To overcome this limitation, radar imagery has emerged as an alternative for flood monitoring (Cao et al., 2019; Adeli et al., 2020; Xie et al., 2023; Amitrano et al., 2024). Unlike optical sensors, radar systems can penetrate cloud cover and operate independently of daylight conditions, making them highly reliable in various weather situations. Additionally, radar sensors provide surface roughness information (Friedman et al., 2012), enabling the distinction between water-covered areas, which exhibit low roughness, and vegetated or urbanized regions with higher roughness (Cao et al., 2019). Many studies use thresholding methods to detect inland water (Cao et al., 2019; Liang et al., 2020; Markert et al., 2020). In this study, we applied a thresholding method called “minimum valley” (Behnamian et al., 2017) enabling the detection of water. We separated flood-water from permanent water bodies using a Digital Elevation Model (DEM) and corrected false detection - corresponding to burnt soil in dry season - using results from a field campaign combined with a burnt soil ratio obtained with optical data (Landsat-8).

While mapping surface water during flood events is essential, estimating water surface elevation (WSE) provides more actionable information, as flow velocity and the extent of infrastructure and crop inundation depend directly on the thickness of the water layer. Current nadir altimetry missions such as Sentinel-3A/B, Jason-3, and Sentinel-6, along with the wide-swath altimetry mission SWOT, now provide reliable measurements of WSE across large water bodies (Crétaux et al., 2017). These observations are essential for improving our understanding

of flood hydrodynamics, enabling more precise modelling, forecasting, and disaster response during flood events.

Building on these advantages, this study uses nine years (2015–2023) of Sentinel-1A radar data to detect floods through a thresholding method and to examine the spatiotemporal dynamics of inundation across the Ouémé floodplain, from seasonal to interannual scales. By integrating radar observations with rainfall analyses, altimetric data, and in-situ measurements, we provide a comprehensive assessment of the hydrological response of the floodplain to flooding events. These findings play a crucial role in enhancing flood prediction capabilities and informing effective flood management strategies in the Ouémé floodplain.

2. Materials and methods

2.1 Study area

Located in southern Benin, West Africa (Fig. 1a), between 6.33°N - 6.50°N and 2.33°E - 2.58°E, the Ouémé floodplain is a vast hydrological system covering approximately 1,500 km² (Fig. 1a). It is composed of two main rivers: the Ouémé and the Sô, both of which are key tributaries of the Nokoué lagoon, the largest water body in Benin (150 km² during low-water periods, Le Barbé et al., 1993). This coastal region forms the southern part of the Ouémé catchment, which extends northwards to the Atacora hills, where the Ouémé river originates (Le Barbé et al., 1993; Lay et al., 2006). The catchment stretches 580 km downstream, where the Ouémé river splits into several branches before flowing into the Nokoué and Porto-Novo lagoons (Moniod et al., 1973).

The Ouémé floodplain begins where the Zou and Ouémé rivers converge (6.99°N 2.40°E) extending about 10 km west of the Ouémé river. The floodplain progressively widens southward reaching nearly 25 km near the Nokoué lagoon. The riverbanks' elevations vary from around 12 m at the connexion of the Ouémé and Zou rivers to 0.4 m at Houédomé, a village near Porto-Novo Lagoon (Le Barbé et al., 1993).

The Sô river, which originates in the northwest of the Ouémé floodplain (6.93°N 2.36°E), at the edge of the Hlan lake (Moniod et al., 1973), runs southward parallel to the Ouémé river. Its riverbanks vary from around 10 m near Hlan lake to 1.3 m at Sô-Ava. The Sô river splits into multiple branches, with its main branch flowing into the Nokoué lagoon accross the Ganvié lacustrine village (Fig. 1b).

The Ouémé and Sô rivers are interconnected by four main branches (Zounga, Agbagbe, Ouovi, Zouvi) that play a key role in the water transportation during overflowing period. When the flow in the Ouémé exceeds a certain threshold, the water either flows into the Sô via tributaries or overflows into the floodplain. Near the Nokoué lagoon, water exchanges between the two rivers occur through wetlands which are inundated during the wet season.

The Ouémé floodplain is relatively flat, with an elevation variation of about 20 m from south to north (Fig. 1c), promoting the spreading of watercourses, erosion, and siltation (Moniod et al., 1973). The Ouémé river has a very gentle slope, with only a 5-meter elevation difference over 85 km from north to south in the floodplain (Le Barbé et al., 1993), and even as little as a few centimetres per kilometre in specific locations (Moniod et al., 1973). This low-lying topography is in favour of agricultural activities but also creates challenges for drainage during the wet season, making it a vulnerability for locals.

Due to variations in the ITCZ position, southern Benin experiences two distinct rainy seasons: the first from April to July when the ITCZ migrates northward, and a shorter one from September to November when the ITCZ returns southward. In contrast, northern Benin, where the ITCZ has a quasi-stationary location in August, experiences a single rainy season. These rains replenish the aquifers that directly feed the Ouémé river at its source (Okpeitcha et al., 2022). Rainfall, estimated to 1,300 mm/year where the Ouémé river originate, and to 1,500 mm/year in the floodplain (Le Barbé et al., 1993), impacts the Ouémé floodplain at varying times and locations. This spatio-temporal variability leads to high river flows between August

and November, causing floods around the Nokoué lagoon and its surrounding watersheds. During this period, the water level in the rivers rise significantly, with flow variations in the Ouémé, ranging from a few tens of m^3/s during low-flow conditions to more than 1,000 m^3/s during flood (Lawin et al., 2019; Morel et al., 2022; Okpeitcha et al., 2022).

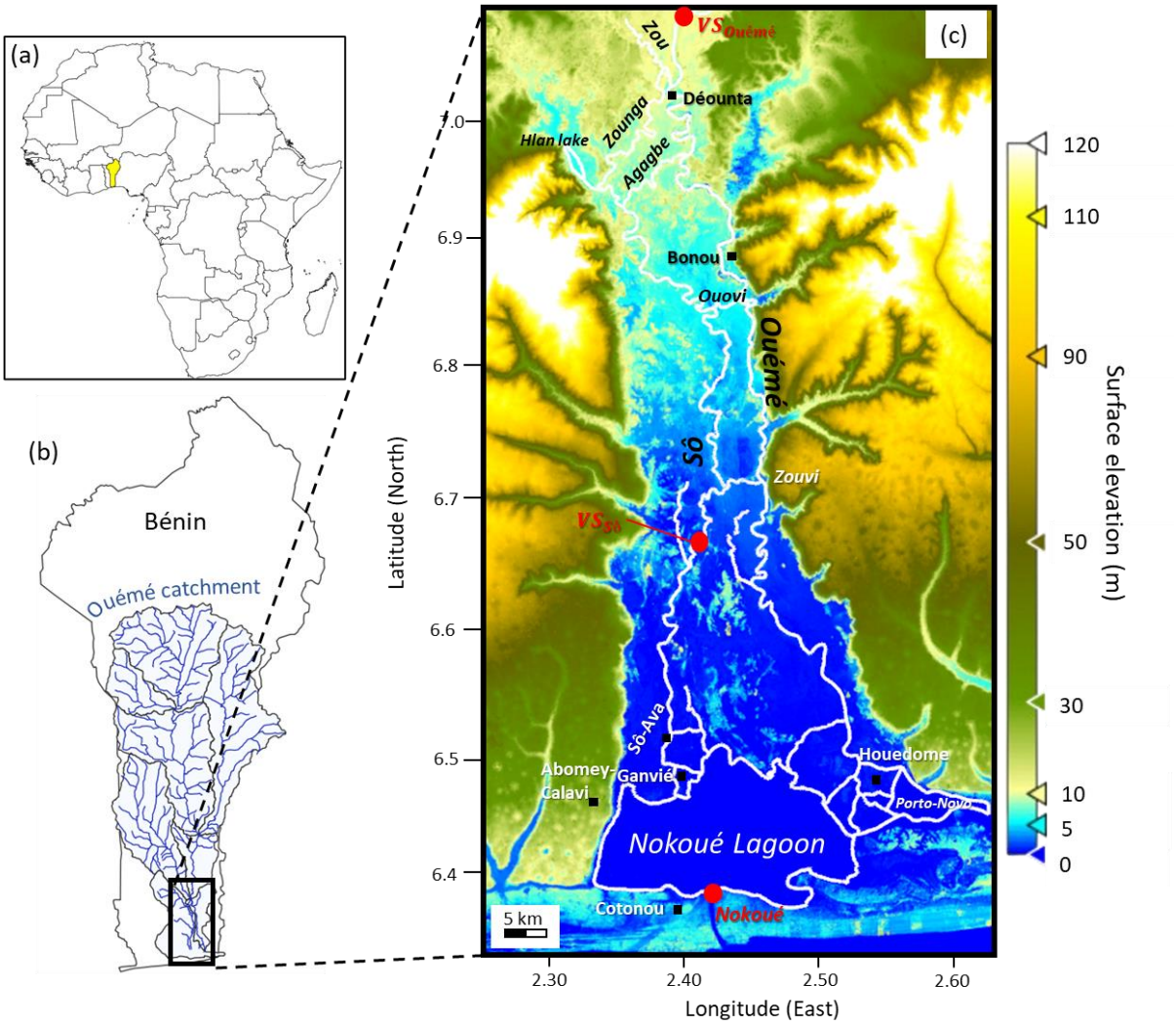

Fig.1 – (a) Localisation of Benin (coloured in yellow) in West Africa. (b) Ouémé catchment in Benin. (c) Topography of the Ouémé floodplain (in meters), red dots indicate in-situ (Ladji) and altimetric virtual stations ($VS_{sô}$ and $VS_{Ouémé}$) for WSE measurements.

2.2 Water surface elevation measurements

Satellite nadir altimetry has become a widely adopted technique for monitoring WSE in inland water bodies such as rivers and lakes (Crétaux et al., 2017). This method provides

measurements at specific locations known as “virtual stations” (VS), where the satellite ground track intersects the riverbed. In this study, two virtual stations are used to monitor water-level variations in the Sô and Ouémé rivers (both VS are available on: hydroweb.next, Santos da Silva et al., 2010; Normandin et al., 2018):

- $VS_{Ouémé}$ is located on the Ouémé river at 7°N 2.4°E (Fig. 1b). Water levels at this location were measured by Jason-2 from August 2008 to May 2016, by Jason-3 from May 2016 to April 2022, and by Sentinel-6 satellites since April 2022, with a temporal resolution of 10 days.
- $VS_{Sô}$ is located on the Sô river at 6.6°N 2.4°E (Fig. 1b), where measurements have been taken by Sentinel-3B every 27 days since December 2018. Water levels variations will be only documented from 2019 to 2023.

Locations of VSs are determined by the satellite ground-tracks, as nadir altimeters only provide measurements at their nadir. Orbit intertrack distance at the equator is equal to 104 km for Sentinel-3B, and to 315 km for Jason-2/3 and Sentinel-6 (that succeeded to each other on the same nominal orbit). This coarse spatial sampling explains why only two VSs could be used in this study.

In addition to satellite measurements, in-situ data are also used. A pressure sensor (HOBO-U20L-01) has been installed since February 2018 in the southern part of Nokoué lagoon (*Ladji,* Fig. 1b) near the entrance of the Cotonou channel. It provides water level data in the lagoon every 20 minutes (Chaigneau et al., 2022, Okpeitcha et al., 2022). These water level measurements are used to analyze both interannual and intra-annual variability, in order to assess the potential maximum WSE in the three water bodies.

2.3 Flooded area detection

2.3.1 Sentinel-1A

In this study, the Sentinel-1A C-band Synthetic Aperture Radar (SAR) sensor is used to detect water-covered areas, particularly flooded areas. This sensor operates independently of weather conditions (e.g., clouds, rain cells) and is capable of capturing images both day and night. The SAR images represent variations in backscatter coefficient, which is the ratio between the power reflected from the surface and the incident power emitted by the radar expressed in decibel (dB). As SAR is a side-looking instrument, these coefficients indicate surface roughness: high backscatter values (bright pixels) typically correspond to rough surfaces such as urban areas or forests, while low values (dark pixels) indicate smoother surfaces like water, due to specular reflection.

Sentinel-1A captures data in two polarization modes simultaneously: VV (vertical transmit and receive) and VH (vertical transmit, horizontal receive). In this study, VV co-polarized images were selected, as they offer better contrast between land and water surfaces (Adeli et al., 2020; Amitrano et al., 2024). Moreover, the 10-meter spatial resolution of Sentinel-1A imagery is well-suited for accurately identifying water-covered areas.

To enable reliable water body detection, several preprocessing steps were applied, including orbit file correction, thermal noise removal, radiometric calibration, speckle noise filtering (using Lee Sigma filter with a 3x3 window (Lee et al., 2015; Kupidura, 2016; Ruben et al., 2021)), range-Doppler terrain correction (using STRM 3Sec as DEM and bilinear interpolation for both resampling method), and conversion to decibel scale (Fig. 2a) (Lee et al., 2009; Filipponi, 2019). The images were processed using European Space Agency (ESA) SNAP software (ESA SNAP, 2015).

With a revisit time of 12 days, a total of 251 raw images were collected between April 2015 and December 2023.

2.3.2 “Minimum valley” thresholding

A widely used method for detecting water pixels in radar images is thresholding, also known as binarization (Adeli et al., 2020; Markert et al., 2020; Amitrano et al., 2024). This approach classifies the pixels of the pre-processed image into two categories based on the distribution of backscatter coefficient values.

In our case, the “minimum valley” thresholding (Behnamian et al., 2017) is applied: the threshold value is determined by automatically identifying the minimum between the two peaks of the image histogram ensuring a well-defined separation between land and water classes. This method is particularly effective when the histogram exhibits a bimodal distribution (Fig. 2b). In this case, the segmented data on the left illustrates the binary classification resulting from the “minimum valley” thresholding applied to the pre-processed radar image, with water pixels represented in black and land pixels in white (Fig. 2c).

In some cases, the histogram does not exhibit a clear bimodal distribution (Fig. 2e), especially for some images acquired during dry season. The threshold is hereby determined by averaging the threshold values of all dry-season images for which the “minimum valley” method applies, as little variations occur during this period. The resulting threshold value was fixed at -14.6 dB.

Some areas among the 251 Sentinel-1 images exhibit a low backscatter coefficient and are incorrectly classified as water (Fig. 2f). These areas, detected as water between December and June, leading to false flood detections, actually correspond to burnt soils, as confirmed during a field campaign in December 2024. In this region, vegetation is often intentionally burned to create arable land, as this practice enriches the soil and clears space for planting (Afira and Wijayanto, 2022). To identify these burnt areas, we used the Normalized Burn Ratio (NBR), which represents the normalized difference between the NIR and SWIR spectral bands (Afira and Wijayanto, 2022). False detections associated with burnt soils appear during the dry season

at the same location with a recurring spatial pattern from year to year. This false detection was confirmed with observations made during the field campaign. It is probably related to both systematic burned soil practice and topographic characteristics of the area. Cloud-free images being rare, to remove this false detection, we computed a NBR mask from a Landsat-8 multispectral image acquired on February 1, 2016 and applied it every year during the dry season. The initial land/water mask was then refined using the NBR index.

Small additional corrections were applied to dry-season data to reduce residual noise (Fig. 2g). Monthly average maps (from January to December, irrespective to the year) were generated to calculate the frequency of water detection for each pixel. Pixels with a water detection rate below 20% were removed to eliminate spurious detections during the dry season.

Furthermore, wind-induced variations in water surface roughness caused some water pixels in Nokoué Lagoon to go undetected. To overcome this, we detected permanent water bodies (the two rivers and the lagoon) in the Ouémé floodplain using the Forest and Building Removal Digital Elevation Model (FABDEM; Hawker et al., 2022). Derived from the Copernicus GLO-30 Digital Elevation Model, FABDEM identifies permanent water bodies as flat surfaces, so that water pixels appear as uniform discrete values, clearly contrasting with surrounding elevations. This characteristic enables straightforward and reliable extraction of pixels associates with permanent water body (Guth et al., 2021).

Finally, to focus exclusively on the floodplain, pixels located above 20 m in elevation were excluded, as these areas lie outside the floodplain (Fig. 1c), resulting in the final product for

water detection for non-bimodal distribution (Fig. 2g).

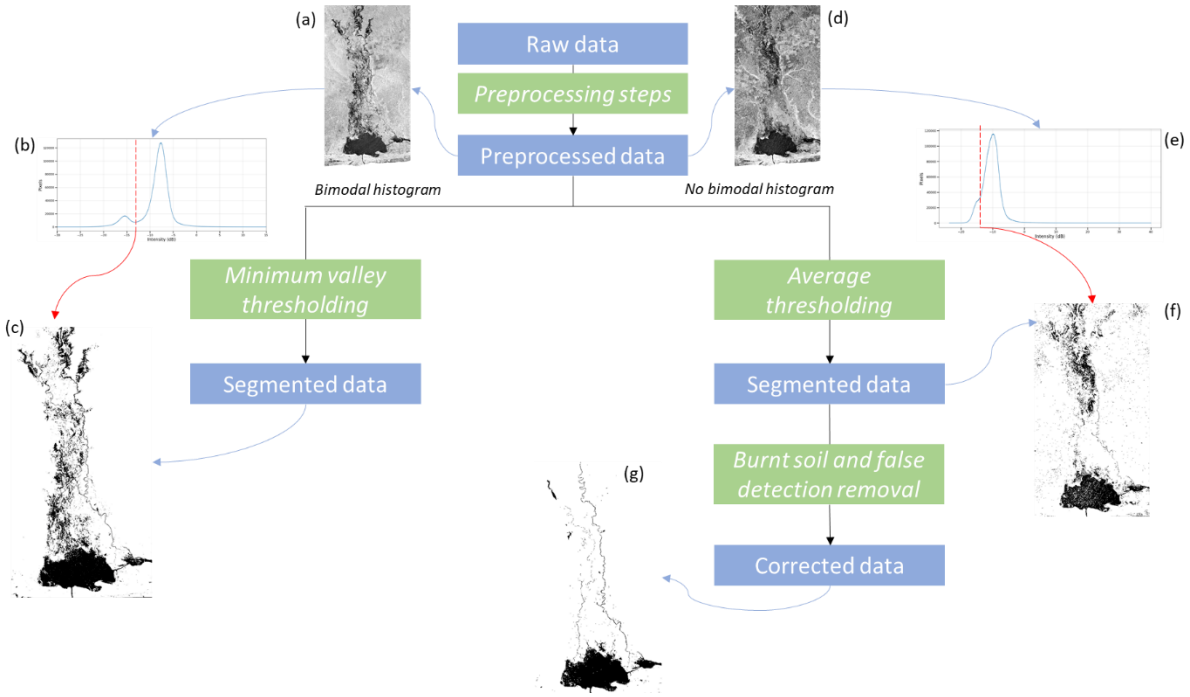

Fig. 2 – Flooded areas detection steps using Sentinel-1A SAR data.

In Section 3.2, we present average monthly maps of flood frequency for the period 2015–2023. For each month, all maps from 2015 to 2023 were considered, and each pixel shows the proportion of times it was detected as flooded. As a result, the monthly frequency maps capture the influence of interannual variability in flooding.

2.2.3 Optical data

Validating Sentinel-1 radar data with optical imagery over the Ouémé floodplain is particularly challenging due to persistent and widespread cloud cover. Although optical sensors such as Sentinel-2 and Landsat-8 share similar spatial and temporal resolutions with Sentinel-1A, their use for validation proved unreliable. The main limitation was the scarcity of cloud-free scenes, with only about a dozen usable images from each sensor between 2015 and 2023.

To overcome this limitation, we used the NOAA VNG Flood V1.0 (VNGF) product, derived from Suomi-NPP/VIIRS optical data (Li et al., 2018), to examine its consistency with flood

detection based on Sentinel-1A. VNGF dataset provides daily observations allowing to construct monthly cloud-free reference images: all cloud-free pixels were aggregated through monthly averaging, as illustrated in Fig. 3. Specifically, for each month of each year, cloud-free pixels were aggregated with other cloud-free observations, while cloudy pixels were excluded. If a given pixel was consistently cloud-covered throughout an entire month, it remained classified as cloud in the monthly image, resulting in the loss of flood information for that location. Also, note that the VNGF product's spatial resolution (375 meters) is considerably coarser than Sentinel-1 SAR imagery (10 meters).

Finally, the VNGF product provides, for each pixel, the fraction of water it contains. Owing to its relatively coarse spatial resolution, a single pixel may contain multiple land-cover types (e.g., water, soil, buildings, vegetation) (Li et al., 2018), so the water fraction represents the proportion of water within that pixel. Flood extent was estimated by summing all pixels containing water weighted by their respective water fraction, while excluding permanent water bodies. This approach produced monthly estimates of flooded areas that can be compared to seasonal patterns of flooding from Sentinel-1 SAR data (Section 4.2).

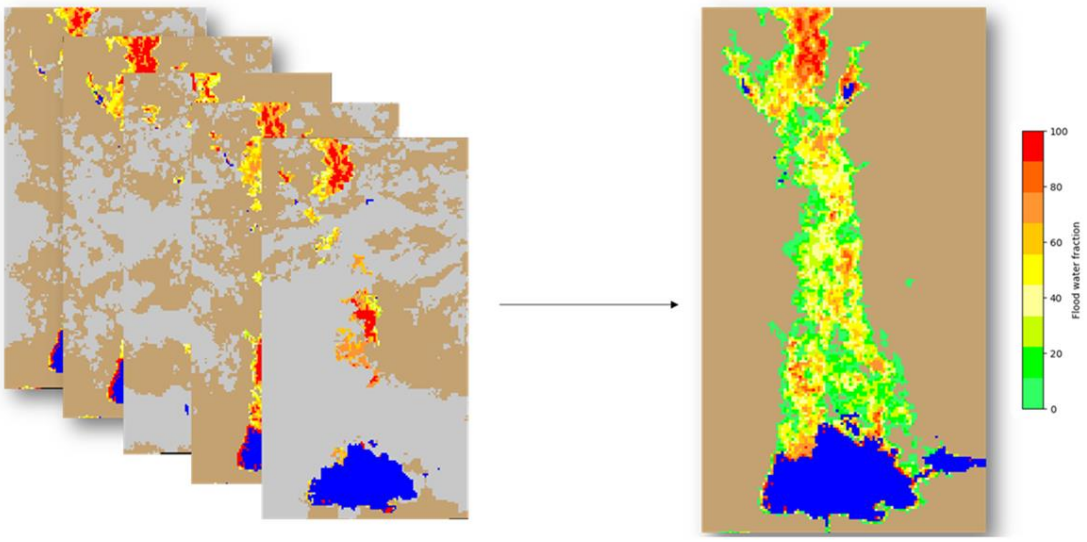

Fig. 3 - Illustration of the averaging process applied to VNGF product (Composite image of September 2018).

2.3 Rainfall data

To assess the contribution of rainfall to flood dynamics, we employed the CHIRPS dataset (Climate Hazards Group InfraRed Precipitation with Station; Funk et al., 2015), which offers high-resolution precipitation estimates (0.05° spatial resolution) by integrating satellite-based observations with ground-based station data. This hybrid approach ensures both spatial coverage and observational accuracy, making it well-suited for hydrological analysis in data-sparse regions.

Rainfall was spatially averaged over the entire Ouémé catchment to reflect basin-scale precipitation conditions, thereby aligning with the scale of the hydrological processes under investigation. To evaluate the reliability of CHIRPS data, we conducted a comparative analysis with in-situ measurements from AMMA-CATCH (Galle et al., 2018) stations, which revealed a strong correlation ($r = 0.8$). This good agreement underscores the validity of the CHIRPS dataset for representing rainfall variability in the region.

3. Results

3.1 Water surface elevation time series

Figure 4a shows WSE variability in the Ouémé river ($VS_{Ouémé}$, Fig. 1b), the Sô river ($VS_{Sô}$, Fig. 1b), and Nokoué lagoon (*Ladji*, Fig. 1b) over the study period, highlighting clear differences in the magnitude and frequency of variations across the three systems.

The Ouémé river shows the largest changes, with WSE varying up to 8 m (red curve). The Sô river has moderate changes, up to 3 m (blue curve), while Nokoué lagoon shows the smallest changes, around 1 m (green curve). Year-to-year differences are also significant. The Ouémé river maximum WSE can vary by up to 2 m between years, the Sô river by about 1 m, and Nokoué lagoon by 0.5 m. Given the relatively large surface area of the lagoon, even small WSE changes correspond to significant volumes of water (approximately 100,000,000 m^3 for a 0.5 m variation).

Figure 4 b-d show a clear seasonal pattern in all three systems, with alternating flood and low-water periods. WSE start rising at different times: in July for the Ouémé river (about +2.5 m), and in August for both the Sô river (+1 m) and Nokoué lagoon (+0.3 m).

Maximal WSE also occur at different times: the Ouémé river peaks in September (6.8 ±1.2 m), while the Sô river (2.5±0.8 m) and Nokoué lagoon (1 ±0.2 m) reach their peak in October. WSE then decrease sharply in November-December and reach their minimum during the dry season.

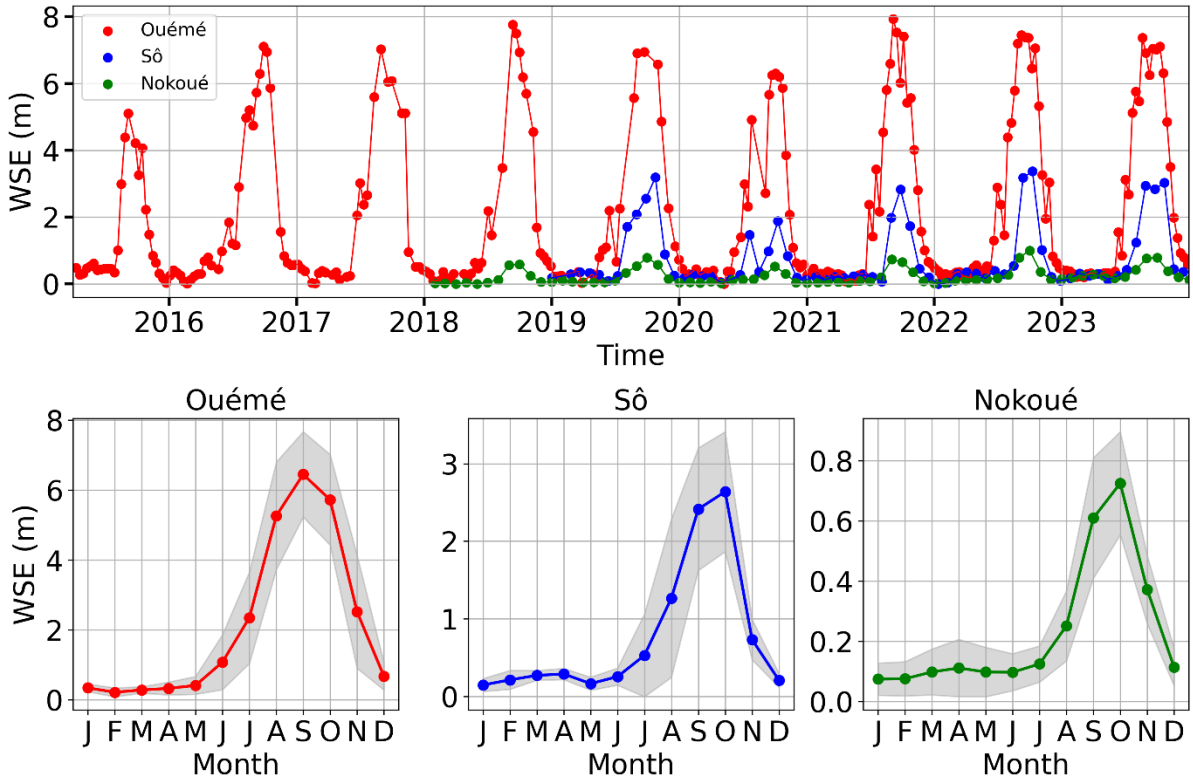

Fig. 4 – Temporal variations in WSE from in-situ measurements and altimetric virtual stations. (a) Interannual WSE dynamics in the Ouémé river (red), the Sô river (blue), and Nokoué lagoon (green). (b - d) Seasonal WSE variations for each site respectively: (b) Ouémé river, (c) Sô river, and (d) Nokoué lagoon. Mean WSE are shown with dotted lines, while gray shaded envelopes represent ±1 STD around the mean seasonal variations.

3.2 Flooded areas

3.2.1 Seasonal variability

The mean seasonal cycle of monthly flood frequency maps, derived from 2015–2023 is shown in Fig. 5, covering the period from July to December.

From December to May (dry season) and May to July (beginning of the wet season), river overflow into the floodplain is very limited and no flooded areas are observed (see July in Fig. 5). During these months, water is confined within the main river channels and small reservoirs.

In August, with the onset of the rainy season in northern Benin, the first floods are observed in the Ouémé floodplain as the rivers swell, overflow and fill reservoirs in the floodplain. On average, flooding during this month is limited, with about 28 km² affected and only small parts of the floodplain inundated. However, low flood frequencies show that flooding can begin earlier in some years, reflecting variability in flood timing.

The flood peak is observed in September, when water spreads widely across the region (Fig. 5). Major overflows occur in the upper Ouémé and lower Sô, with flood percentage frequencies reaching around 50% along the Sô river, where several villages are located. This zone was regularly flooded throughout the study period, highlighting its persistent flood exposure. On average, the mean flooded extent reaches about 55 km². During this peak period, floodwaters flow through all four hydrological connections located between the two rivers (see Fig. 1b), and inundate the intermediate wetlands.

By October, floods begin to recede, with the mean inundated area decreasing by about 44 km², particularly in the northern Ouémé. However, high flood frequencies (up to 70%) persist along the Sô river, indicating a northeast to southwest spreading of the flooded area and the persistency of the flood in the southwest of the floodplain in October, regardless of the year.

In November, the situation is similar to August in the southwest of the floodplain, with a decrease of flooded areas down to 19 km² and rivers returning to their usual channels in the northern area. These observations are consistent with the water level patterns described in Section 3.1, confirming that the main flood season extends from August to November.

The largest flooded surfaces correspond to pixels with a relatively low occurrence frequency (<20%), with a maximum in September where more than 120 km² are temporarily inundated. This reflects the broad but episodic extent of seasonal floods. In contrast, pixels that are more regularly flooded (>50%) cover only relatively small areas, indicating that only a few restricted parts of the floodplain are subject to nearly permanent inundation. Seasonality is clear, with

flooding starting in August, peaking in September, and gradually receding in October-November before almost disappearing in December. This distribution highlights the contrast between extensive areas flooded episodically and small, consistently inundated areas.

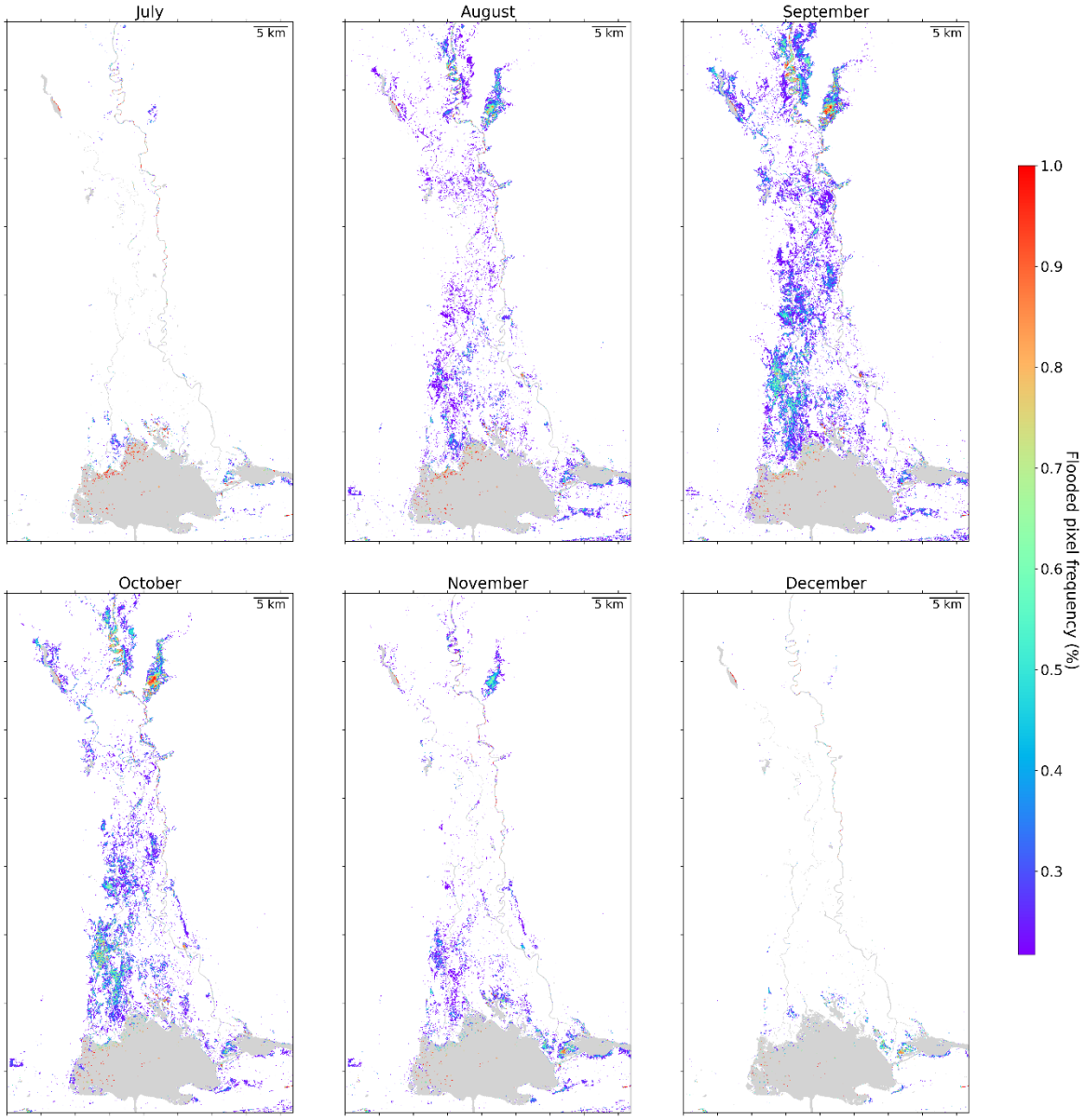

Fig. 5 – Mean monthly flood frequency maps (July–December, 2015–2023). For each map frequencies (in %) were computed from 17 to 23 satellite images collected between 2015 and 2023. Flood-prone areas are shown in colour, while permanent water bodies are displayed in light grey.

3.2.2 Interannual variability

In addition to strong seasonal variation, flooded areas also exhibit interannual variability, reflecting a complex hydrological regime (Fig. 6a, blue curve). From 2015 to 2017, flooded areas remained relatively stable (~30–40 km²), followed by a significant peak in 2018 (~100 km²). Subsequent years showed irregular patterns, with notable extremes in 2021 (~110 km²) and 2022 (~160 km²), before declining to ~70 km² in 2023. Despite this irregularity, Fig. 6a shows a general trend of increasing flood extent over the study period, confirmed by a statistical analysis ($p=0.03<0.05$). Thus, despite the short time series, peak flood extent has increased significantly over the study period with a mean rate of 6 km^2/year. Finally, flood peak timing also varies, such as the 2020 peak occurring nearly a month earlier than in 2022.

This interannual variability mainly results from the floodplain's response to rainfall (Fig. 6a, grey bars). However, a closer examination reveals that it is not only the rainfall immediately prior to the flood peak that determines flood magnitude. For example, rainfall in the two months before the 2021 flood peak was higher than in 2022, yet the flood peak in 2022 exceeded that of 2021.

To better understand the rainfall–flood mechanism, we analysed the flood response to cumulative rainfall over different periods. Our analysis indicates that the period from January to September is the most representative of this mechanism. Specifically, we compared the cumulative rainfall over the January-September period for each year with the corresponding maximum flooded area (reached in or after September, Fig. 6b). This approach ensures that only rainfall occurring prior to the flood peak is considered, providing a clear link between rainfall patterns and flood extent. Rainfall accumulation during the previous dry and wet seasons plays a key role, as it replenishes wetlands, refills aquifers, and saturates soils, thereby creating the hydrological conditions that allow subsequent rainfall to translate into extensive flooding.

The results also reveal significant interannual variability in rainfall across the study period (Fig. 6b). In 2015, total rainfall barely reached 800 mm, making it the driest year, which coincided with a minimal flooded area extent of less than 30 km². In contrast, 2022 recorded the highest total rainfall (~1,200 mm), which was associated with the largest flooded area extent (160 km²). Finally, the strong rainfall–flooding relationship illustrated in Fig. 6b, exhibits a distinct threshold: below ~1,070 mm of cumulative rainfall, flood extent remains under 40 km², whereas above this threshold, flood extent increases roughly proportionally with cumulated rainfall. Even though a strong interannual variability exists in the rainfall pattern, rainfall follow a significant upward trend ($p = 0.02 < 0.05$).

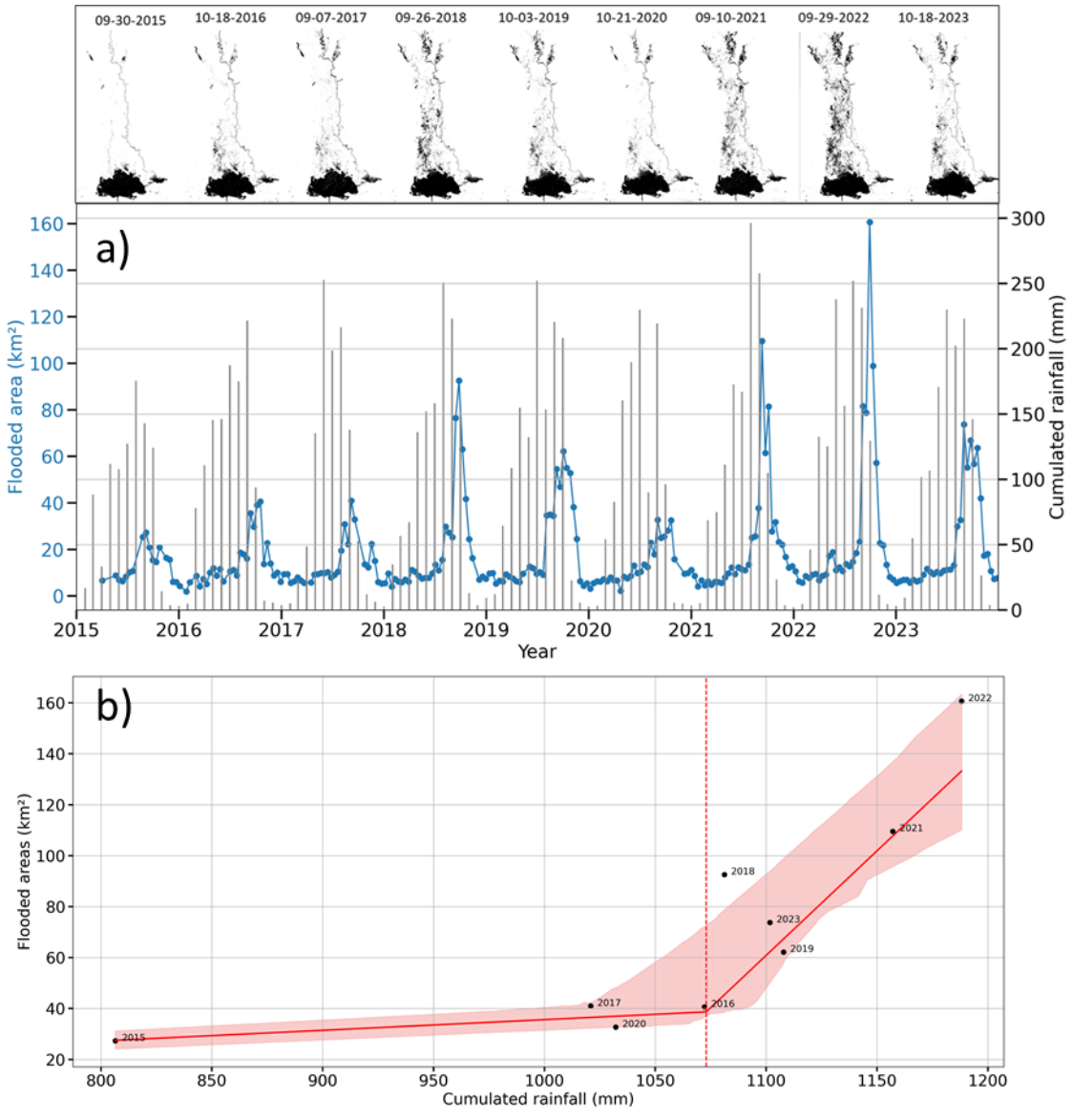

Fig. 6 – a) Temporal evolution of flooded areas over 2015–2023 period (blue dotted line, left axis) and monthly cumulated rainfall (grey bars, right axis). Sentinel-1A water masks corresponding to the maximum annual flood are shown above with the corresponding date. b) Relationship between cumulative rainfall (January-September) over the Ouémé catchment and annual flood peaks. Black dots represent annual observations (2015-2023). Red lines indicate the best-fit linear regressions, with shaded areas representing the 95% confidence intervals derived from bootstrapping. The red dotted line marks the rainfall threshold that best separate the two regimes discussed in the text.

3.3 Relationship between flooded areas and WSE in rivers and Nokoué lagoon

In the Ouémé floodplain, floods occur primarily due to river overflows, when rivers carry a large volume of water during the wet season. In order to estimate the river WSE threshold that induce flooding, we analyse the relationship between the extent of flooded areas and WSE in both rivers and in Nokoué lagoon (Fig. 7).

In the Ouémé river, two distinct regimes are observed (Fig. 7a). When the water remains confined within the riverbed, the WSE can rise up to about 6 m, while the flooded areas remain below 30 km². Once the WSE variation exceeds 6 m – corresponding to an absolute water level of 12 m-, the flooded areas expand significantly. This 6-meter overflow likely corresponds to the Ouémé overtopping riverbanks, as mentioned in Section 2.1.

In the Sô river, a more linear pattern is observed (Fig. 7b). The flooded area extent begins to increase significantly once WSE variations exceed 0.5 m, signaling the onset of overflow. In contrast to the Ouémé river, overflows in the Sô are triggered at much lower WSE, largely due to the low elevation of its riverbanks, which are generally less than 1 m above the riverbed (see Section 2.1). As WSE surpasses 3 m, the flooded area reaches its maximum extent.

In comparison, the Nokoué lagoon displays a less linear relationship between flooded area extent and WSE variation, with a clear threshold near 0.25 m (Fig. 7c).

This behavior reveals the varying flood responses across the system and the importance of knowing local thresholds to understand and anticipate flood events.

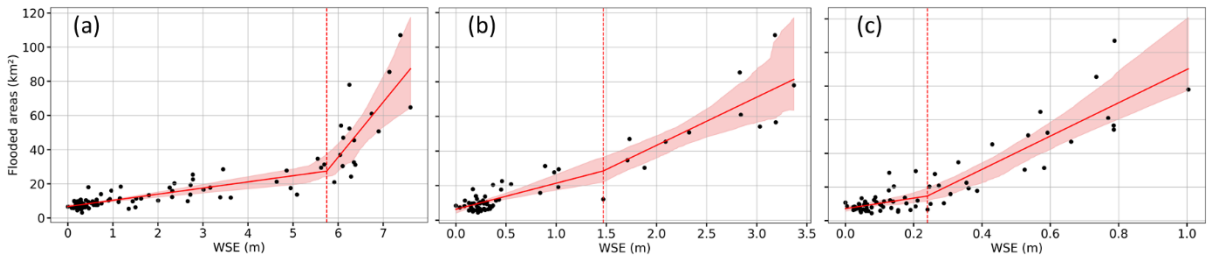

Figure 7 - Relationship between the extent of flooded areas and WSE in (a) Ouémé river, (b) Sô river and (c) Nokoué lagoon. Black dots represent individual observations from 2015 to 2023. Red lines indicate the best-fit linear regressions, with shaded envelopes representing the 95% confidence intervals derived from bootstrapping. Red dotted lines mark the WSE thresholds that best separate the two linear regimes.

4 Discussion

4.1 Rainfall-flood extent relationship and the role of hydrological connectivity in the Ouémé floodplain

In Section 3.2.2, we highlighted a global relationship between flooded area extent and cumulative January–September rainfall, with two distinct regimes. Below ~1070 mm of cumulated rainfall, inundation remains limited to about 40 km², whereas a sharp increase in flooded area is observed above this threshold. However, the relationship, is not strictly linear. While the overall trend indicates that higher precipitation generally leads to larger inundated areas, some interannual discrepancies are observed (Fig. 6b). Several processes may contribute to these differences. For instance, antecedent hydrological conditions such as soil moisture, groundwater levels, or reservoir storage influence the extent of inundation even under slightly

lower seasonal rainfall. Likewise, the intra-seasonal distribution of rainfall may play a role, since a few intense events concentrated in time can generate more extensive flooding than similar cumulative rainfall distributed more evenly. The synchronization of peak flows from different tributaries may also affect the magnitude of floodplain inundation.

In addition, geomorphological changes or human activities may contribute to modifying the rainfall–flood relationship. Variations in river channel and floodplain morphology, sediment deposition, vegetation, or the operation of hydraulic structures could influence the capacity of the floodplain to store and convey water. External factors such as downstream water levels or climatic conditions (e.g., evapotranspiration) might also play a part. These potential processes could explain why, in some years, slightly lower rainfall still coincided with larger inundated surfaces, underlining the complexity of flood dynamics.

Beyond rainfall alone, the spatial distribution of flooded areas is closely linked to the hydrological connections within the basin (Section 2.1). The high frequency of flooding along the Sô River (Fig. 8) indicates that a significant portion of water flows through this area during the wet season, mainly originating from the Ouémé river via several connecting channels. Among these, the Zuovi channel is the primary hydrological link (see Section 2.1, Fig.1), while additional reservoirs and smaller channels (red circle Fig. 8) further enhance connectivity. Flood propagation appears to follow a south-westward trajectory, moving from one reservoir to another, with detection frequencies increasing along the path (as shown in Fig. 4 “September”). These connections are facilitated by the low topography and riverbank elevations, which allow flood propagation across the floodplain. Section 3.3 further supports this interpretation: the sharp increase in flooded areas along the Sô River, despite only a slow rise in WSE, indicates that a large volume of water enters the river and overflows almost immediately due to the low banks. However, accurately characterizing the Sô river response to the incoming water remains difficult due to the absence of long-term in-situ data or the limited

availability of altimetry, with measurements available only every 27 days for the Sô river, compared to 10-day intervals for the Ouémé river. This disparity makes it difficult to establish a precise correlation between WSE fluctuations and the spatial extent of flood in the Sô region.

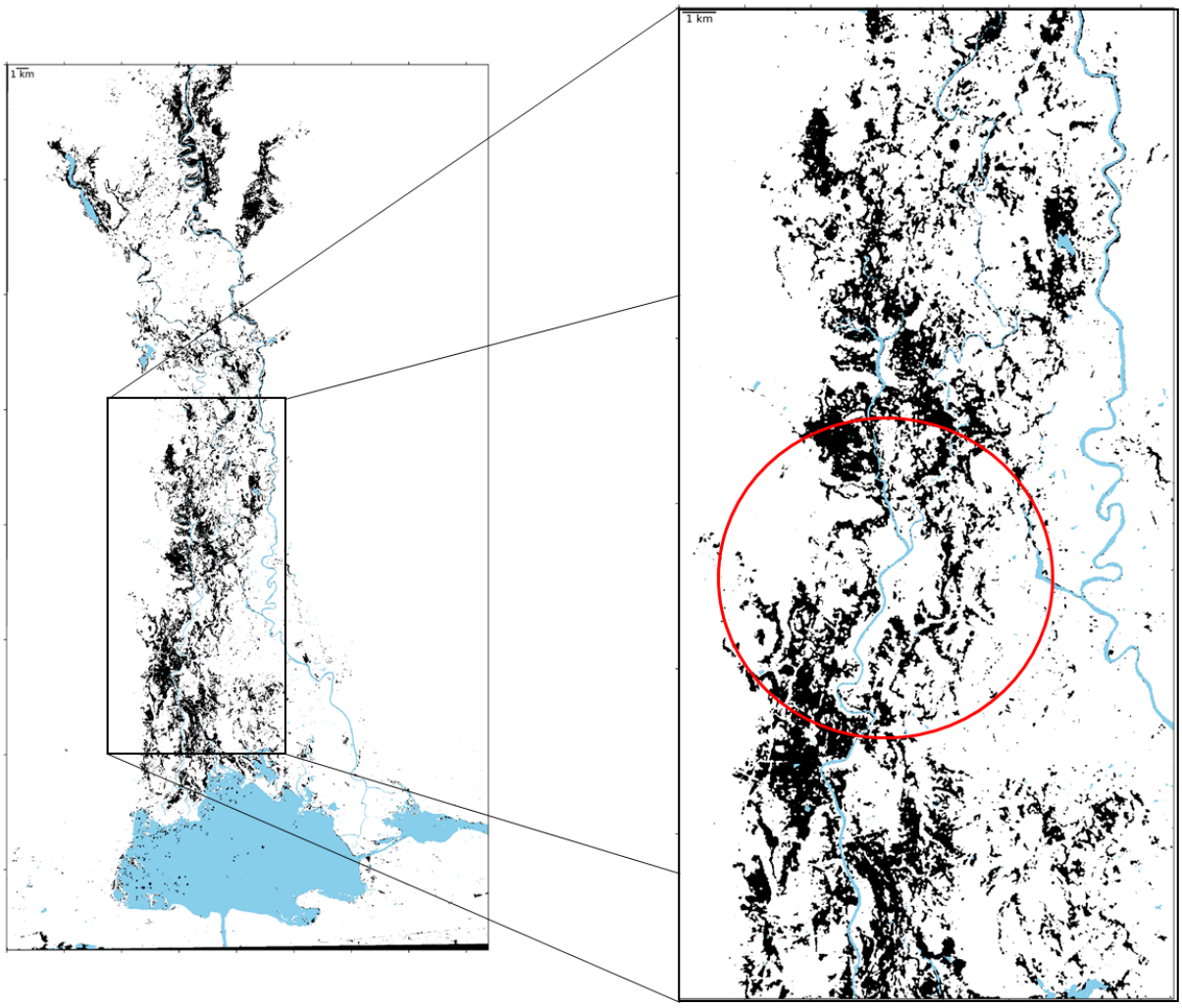

Figure 8 - Zoom on the flood-prone areas along the Sô river during the major flood of 2022, showing the flood reservoirs and their connections (red circle). Flooded areas are represented in black and permanent water bodies in blue.

4.2 Comparisons with VNGF product

Figure 9 compares the previous flood extent evolution (Fig. 6a and blue curve in Fig. 9) to estimates from the VNGF product. The seasonal patterns are consistent with both datasets showing increased flood extents during wet seasons and decreases during dry periods. However,

strong quantitative differences are observed. At the beginning of the study period, particularly between 2015 and 2017, the VNGF product failed to capture flooding. A detailed inspection of VNGF images shows this is likely due to persistent cloud cover: less than 5 images were usable during the flood season each year. In contrast, Sentinel-1 sensor successfully detected flooded areas during these three years. This pattern reversed in 2018 and 2019, when the VNGF product estimated significantly more flooded area than Sentinel-1—up to 100 km² more in 2018 and about 70 km² in 2019. The situation flipped again in 2021 and 2022, when Sentinel-1 detected more extensive flooding than VNGF, by roughly 30 km². Interestingly, the years 2020 and 2023 displayed the highest consistency between both sources. Some discrepancies were also observed during dry periods, possibly due to differences in sensor sensitivity and spatial resolution.

Overall, despite its potential, the comparison highlights the limitations of VNGF product to evaluate flood extent, particularly under challenging atmospheric conditions. Radar data from Sentinel-1 proves to be the most relevant source for this region, thanks to its ability to penetrate cloud cover and deliver consistent flood mapping, especially critical during the wet season.

Validation of Sentinel-1 SAR flood products using independent data in our study area is thus a challenge. However, the consistency of the flood patterns at seasonal and interannual timescales, together with the consistency of the relationship with river elevation and cumulative rainfall variations, provide strong support for the overall validity of our analysis.

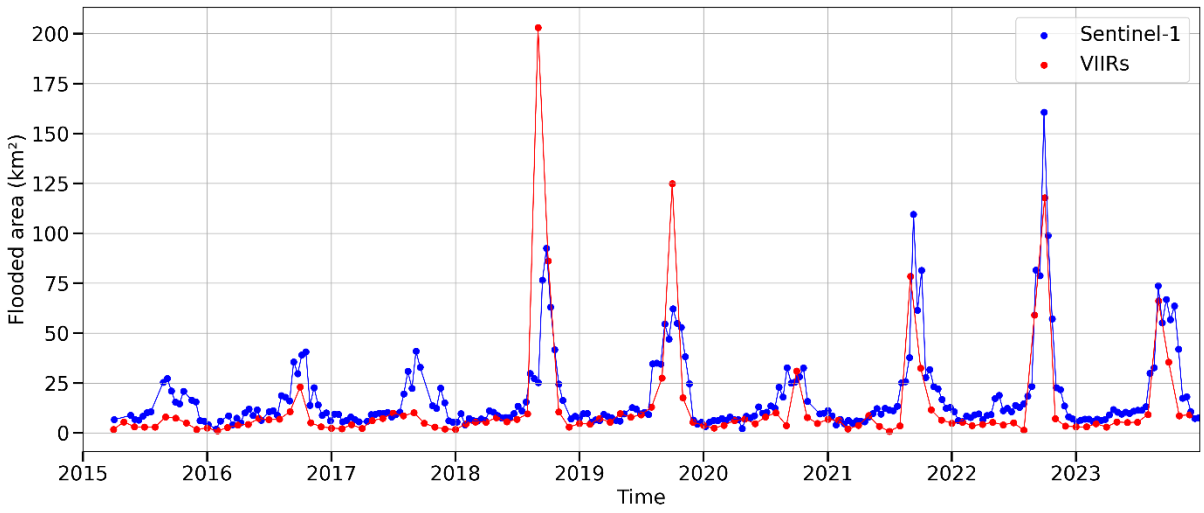

Fig. 9 – Time series of the extent of flooded areas derived from Sentinel-1 (shown in blue) and VNGF (shown in red).

5 Conclusion

In this study, we investigated the spatio-temporal variability of water-covered areas in the Ouémé floodplain by combining satellite altimetry, in situ measurements and Sentinel-1A radar imagery.

The analysis revealed significant WSE fluctuations—approximately 1 m in the Nokoué lagoon, 3.5 m in the Sô river, and up to 8 m in the Ouémé river. When the Ouémé river WSE rises by 5–6 m from its low-water level, it induces significant overflows feeding the floodplain, triggering the seasonal flooding observed between August and November and establishing a connection with the Sô river. Flooded areas range on average from 20 km^2 in the dry season up to 160 km^2 during flood peaks, with a strong interannual variability (30-160 km^2) closely linked to cumulative rainfall (January-September). Flood frequency maps further revealed recurrently inundated zones, underscoring areas of persistent exposure in the southwest of the areas. Finally, results highlight a significant upward trend in flooded areas over 2015–2023, with an average annual increase of about 6 km^2, indicating a progressive intensification of flooding during the study period.

The study also highlights the strengths and current limitations of satellite monitoring. The current 12-day revisit cycle of Sentinel-1A could be complemented by higher-frequency observations through multi-satellite integration to better capture the rapid dynamics of flood events. The 10-meter spatial resolution offers a solid foundation for detailed mapping, but further improvements could be achieved in densely urbanized areas where radar signal is often affected by infrastructure. In this study, only VV and VH polarization data were available, but the inclusion of horizontal co-polarization (HH) in future datasets may further improve water surface detection.

Additionally, while C-band radar is effective for open water detection, integrating sensors with longer wavelengths, such as L-band SAR, could enhance the ability to detect water under dense vegetation—an important consideration in wetland-dominated environments like the Ouémé floodplain. Incorporating altimetry data and high-resolution Digital Elevation Models (DEMs) would also allow for more accurate estimation of flood depth and volume, particularly in flat and low-lying regions.

The interconnectivity of rivers, wetlands, and the lagoon system, combined with the flat topography, makes the hydrological behaviour of the area particularly complex. A fully integrated framework, bringing together radar and optical remote sensing, altimetry, DEM analysis, and field observations, is crucial to enhance the spatial precision and temporal reliability of flood monitoring.

Ultimately, this work provides useful metrics for the calibration of a hydrological model aimed at predicting flood-prone areas across the Ouémé floodplain. Based on satellite-derived data, we demonstrated that once specific water surface elevation thresholds are exceeded, the Ouémé and Sô rivers systematically overflow into the surrounding floodplain. We also highlighted the strong seasonality of inundated areas and established a clear relationship between cumulative rainfall (January–September) and the spatial extent of flooding. Flood frequency maps further

revealed recurrently inundated zones, underscoring areas of persistent exposure. Together, these findings represent a key contribution to regional flood management and risk mitigation, and open new perspectives for future advances in satellite-based hydrology. First, the systematic link between rainfall accumulation, elevation thresholds, and flood extent could be further explored and integrated into early warning systems, providing physically based triggers for flood onset in the data-scarce Ouémé floodplain. Second, coupling flood frequency maps with land-use and population data would allow the development of vulnerability maps, supporting risk prioritization and community adaptation planning. More generally, extending this approach to include socioeconomic datasets and hydrodynamic modelling could strengthen the basis for operational flood forecasting and long-term management strategies.

Acknowledgments

This research is a contribution to the "Lagune Nokoué" TOSCA project and the “Space Climate Observatory” SCOast-DT program, both funded by the French National Center for Space Studies (CNES). Noémie Ferdinand is funded by a University of Toulouse PhD grant. We warmly thank A. Assogba and J. Honfo for their support during the field campaign in the Ouémé wetlands.

References

Adeli, S., Saheli, B., Mahdianpari, M., Quackenbush, L.-J., Brisco, B., Tamiminia, H., Shaw, S. (2020). Wetland Monitoring Using SAR Data: A Meta-Analysis and Comprehensive Review. *Remote Sensing,* 12(14), 2190, https://doi.org/10.3390/rs12142190.

Afira, N., Wijayanto, A. (2022). Mono-temporal and multi-temporal approaches for burnt area detection using Sentinel-2 satellite imagery (a case study of Rokan Hilir Regency, Indonesia). *Ecological Informatics,* 69, https://doi.org/10.1016/j.ecoinf.2022.101677.

Ahouangan, M.-B, Djaby, B., Ozer, P., Hountndji, Y.-C., Thiry, A., De Longueville, F. (2014). Adaptation et résilience des populations rurales face aux catastrophes naturelles en Afrique subsaharienne. Cas des inondations de 2010 dans la commune de Zagnanado, Bénin.

Amitrano, D., Di Martino, G., Di Simone, A., Imperatore, P. (2024). Flood Detection with SAR: A Review of Techniques and Datasets. *Remote Sensing* 16.4, 656, https://doi.org/10.3390/rs16040656.

Amoussou, E., Amoussou, F., Bossa, A., Kodja, D., Vodounon, H., Houndénou, C., Estupina, V., Paturel, J.-E., Mahé, G., Cudennec, C., Boko, M. (2024). Use of HEC RAS model for the analysis of exceptional floods in the Ouémé basin. *Hydrological science in anthropocène,* 385, 141-146, https://doi.org/10.5194/piahs-385-141-2024.

Behnamian, A., Banks, S., White, L. Brisco, B., Millars, K., Pasher, J., Chen, Z., Duffe, J., Bourgeau-Chavez, L., Battaglia, M. (2017). Semi-automated surface water detection with synthetic aperture radar data: a wetland case study. *Remote sensing, 9,* 1209. https://doi.org/10.3390/rs9121209.

Bossa, Y.A., Djangni, O., Yira, Y., Hounkpè J., Avossè, A.D., Sintondji, L.O. (2024). Flood risk assessment in the lower valley of Ouémé, Benin. *Open Journal of Modern Hydology*,14, 130-151. https://doi.org/10.4236/ojmh.2024.142008.

Brakenridge, R., Anderson, E. (2006). Modis-based flood detection, mapping and measurement: the potential for operational hydrological application. *Transboundary Floods: Reducing Risks Through Flood Management*, 1–12, https://doi.org/10.1007/1-4020-4902-1_1.

Cao, H., Zhang, H., Wang, C., Zhang, B. (2019). Operational Flood Detection Using Sentinel-1 SAR Data over Large Areas. *Water* 11.4, 786, https://doi.org/10.3390/w11040786.

Chaigneau, A., Stieglitz, T., Okpeitcha, V., Assogba, A., Sohou, Z., Peugeot, C., Morel, Y. (2020). Impact du changement global sur les systèmes lagunaires en Afrique de l'Ouest : le cas du lac Nokoué au Bénin. *Météo et Climat Info*, 79, 2-3, ⟨hal-03365173⟩.

Chaigneau, A, Okpeitcha, V., Morel, Y., Stieglitz, T., Assogba, A., Benoist, M., Allamel, P., Honfo, J., Derol Awoulmbang Sakpak, T., Rétif, F., Duhaut, T., Peugeot, C., Souhou, Z. (2022). From seasonal flood pulse to seiche: Multi-frequency water- level fluctuations in a large shallow tropical lagoon (Nokoué Lagoon, Benin)". *Estuarine, Coastal and Shelf Science* 267, 107767, https://doi.org/10.1016/j.ecss.2022.107767.

Conway, D. (2004). Extreme Rainfall Events and Lake Level Changes in East Africa: Recent Events and Historical Precedents. *The East African Great Lakes: Limnology, Palaeolimnology and Biodiversity*. 63–92, http://dx.doi.org/10.1007/0-306-48201-0_2.

Crétaux J.-F., Nielsen, K., Frappart, F., Papa, F., Calmant, S. and Benveniste, J. (2017). Hydrological applications of satellite altimetry: rivers, lakes, man-made reservoirs, inundated areas. *Satellite Altimetry Over Oceans and Land Surfaces, Earth Observation of Global Changes*, 459-504, http://dx.doi.org/10.1201/9781315151779-14

Di Baldassarre, G., Montanari, A., Lins, H., Koutsoyiannis, D., Brandimarte, L., Blöschl, G. (2010). Flood fatalities in Africa: From diagnosis to mitigation. *Geo-physical Research Letters*, 37.22, http://dx.doi.org/10.1029/2010GL045467.

Dore, M. H. I. (2005). Climate change and changes in global precipitation patterns: What do we know? *Environment International* 31.8, 1167–1181, https://doi.org/10.1016/j.envint.2005.03.004.

Du, Y., Zhang, Y., Ling, F., Wang, Q., Li, W., Li, X. (2016). Water Bodies' Mapping

from Sentinel-2 Imagery with Modified Normalized Difference Water Index at 10-m Spatial Resolution Produced by Sharpening the SWIR Band. *Remote Sensing* 8.4, https://doi.org/10.3390%2Frs8040354.

ESA SNAP Software. 2025. "SNAP download." https://step.esa.int/main/download/snap-download/.

Filipponi, F. (2019). Sentinel-1 GRD Preprocessing Workflow. *Proceedings* 18.1, https://doi.org/10.3390%2FECRS-3-06201.

Friedman, A., Pizarro, O., Williams, S.B., Johnson-Roberson, M. (2013) Correction: Multi-Scale Measures of Rugosity, Slope and Aspect from Benthic Stereo Image Reconstructions. *PLOS ONE* 8(12), https://doi.org/10.1371/journal.pone.0050440.

Funk, C., Peterson, P., Landsfeld, M., Pedrerod, D., Verdin, J., Shukla, S. Husak, G., Rowland, J. Harrison, L., Hoell, A., Michaelsen, J., 2015. The climate hazards infrared precipitation with stations—a new environmental record for monitoring extremes, *Scientific Data, 2,* https://doi.org/10.1038/sdata.2015.66.

Galle et al., 2018. AMMA-CATCH a critical zone observatory in West Africa monitoring a region in transition. *Vandose Zone Journal, 17 (1),* 1-24. https://doi.org/10.2136/vzj2018.03.0062.

Government of the Republic of Benin, World Bank, United Nations, 2011. Flooding in Benin, Post-catastrophic need assessment report.

Guth, P., L., Van Niekerk, A., Grohmann, C., H., Muller, J.-P., Hawker, L., Florinsky, I., V., Gesch, D., Reuter, H., I., Herrera-Cruz, V., Riazanoff, S., Lopez-Vazquez, C., Carabajal, C., C., Albinet, C., Strobl, P. (2021). Digital Elevation Models : Terminology and Defintions. *Remote Sensing 13(18) 3581.* https://doi.org/10.3390/rs13183581

Hawker, L., Uhe, P., Paulo, L., Sosa, J., Savage, J., Sampson, C. Neal, J. (2022). A

671 30 m global map of elevation with forests and buildings removed. *Environmental*
672 *Research Letters* 17.2., https://doi.org/10.1088/1748-9326/ac4d4f.
673 Hounkpè, J., Diekkrüger B., Badou, D.F., Afouda, A.A. (2015). Non-stationary flood
674 frequency analysis in the Ouémé river basin, Benin Republic. *Hydrology 2015*, 2, 210-
675 229. https://doi.org/10.3390/hydrology2040210.
676 Ji, L., Geng, X., Sun, K., Zhao, Y., Gong, P. (2015). Target Detection Method for Water
677 Mapping Using Landsat 8 OLI/TIRS Imagery. *Water* 7.2., 794–817.,
678 https://doi.org/10.3390/w7020794.
679 Junk, W.J., Welcomme, R.L. (1990) Floodplains. *Wetlands and Shallow Continental*
680 *Water Bodies*, pp. 491–524.
681 Kupidura, P., 2016. COMPARISON OF FILTERS DEDICATED TO SPECKLE
682 SUPPRESSION IN SAR IMAGES. *The International Archives of the Photogrammetry,*
683 *Remote Sensing and Spatial Information Sciences* XLI-B7, 269–276.
684 https://doi.org/10.5194/isprs-archives-XLI-B7-269-2016
685 Lawin, A.-E., Hounguè R., N'Tcha M'Po, Y., Rholan Hounghè, N., Attogouinon, A.,
686 Afouda, A.-A. (2019). Mid-century climate change impacts on Ouéme river discharge at
687 Bonou outlet (Bénin). *Hydrology* 6, https://doi.org/10.3390/hydrology6030072.
688 Le Barbé, L., Alé, G., Texier, H., Borel, Y., & Gualde, R. (1993). Les ressources en eaux
689 superficielles de la République du Bénin. *Monographies hydrologiques*.
690 Lee, J.-S., Wen, J.-H., Ainsworth, T.-L., Chen, K.-S., Chen, A.-J. (2009). Improved
691 Sigma Filter for Speckle Filtering of SAR Imagery. *IEEE Transactions on Geoscience*
692 *and Remote Sensing* 47.1, 202–213, https://doi.org/10.1109/TGRS.2008.2002881.
693 Lee, J.-S., Ainsworth, T.L., Wang, Y., Chen, K.-S., 2015. Polarimetric SAR Speckle Filtering
694 and the Extended Sigma Filter. *IEEE Transactions on Geoscience and Remote Sensing*
695 53, 1150–1160. https://doi.org/10.1109/TGRS.2014.2335114

Le Lay, M., (2006). Modélisation hydrologique dans un contexte de variabilité hydro-climatique. Une approche comparative pour l'étude du cycle hydrologique à méso-échelle au Bénin." PhD thesis. Institut National Polytechnique de Grenoble – INPG, https://theses.hal.science/tel-00116912.

Li, S., Sun, D., Goldberg, M.-D., Sjoberg, B., Santek, D., Hoffman, J.-P., DeWeese, M., Restrepo, P., Lindsey, S., Holloway, E. (2018). Automatic near real-time flood detection using Suomi-NPP/VIIRS data. *Remote Sensing of Environment* 204, 672–689, https://doi.org/10.1016/j.rse.2017.09.032.

Liang, J., Desheng, L (2020). A local thresholding approach to flood water delineation using Sentinel-1 SAR imagery. *Journal of Photogrammetry and Remote Sensing*, 159, 53-62. https://doi.org/10.1016/j.isprsjprs.2019.10.017.

Markert, K.-N., Markert, A.-M., Mayer, T., Nauman, C., Haag, A., Poortinga, A., Bhandari, B., Soe Thwal, N., Kunlamai, T., Chishtie, F., Kwant, M., Phongsapan, K., Clinton, N., Towashiraporn, P., Saah, D. (2020). Comparing Sentinel-1 Surface Water Mapping Algorithms and Radiometric Terrain Correction Processing in Southeast Asia Utilizing Google Earth Engine. *Remote Sensing* 12.15, p. 2469, https://doi.org/10.3390/rs12152469.

Moniod, F. (1973). Régime hydrologique de I'Ouémé (Dahomey).

Morel, Y., Chaigneau, A., Okpeitcha, V., Stieglitz, T., Assogba, A., Duhaut, T., Rétif, F., Peugeot, C., Sohou, Z. (2022). Terrestrial or oceanic forcing? Water level variations in coastal lagoons constrained by river inflow and ocean tides. *Advances in Water Resources* 169, https://doi.org/10.1016/j.advwatres.2022.104309.

Normandin C. Frappart F., Diepkile A.T., Marieu V., Mougin E., Blarel F., Lubac B.,

Braquet N., Ba A. (2018). Evolution of the Performances of Radar Altimetry Missions from ERS-2 to Sentinel-3A over the Inner Niger Delta. *Remote Sensing*, 10(6), 833, https://doi.org/10.3390/rs10060833

Okpeitcha, V., Chaigneau, A., Morel, Y., Stieglitz, T., Pomalegni, Y., Sohou, Z., Mama, D. (2022). Seasonal and interannual variability of salinity in a large West-African lagoon (Nokoué Lagoon, Benin). *Estuarine, Coastal and Shelf Science* 264, https://doi.org/10.1016/j.ecss.2021.107689.

Otsu, N. (1979). A threshold selection method from gray-level histograms. *Transactions on Systems, Man and Cybernectics, 9,* 62-66. https://doi.org/10.1109/TSMC.1979.4310076.

Pekel, J.-F., Cottam, A., Gorelivk, N., Belward, A.-S. (2016). High-resolution mapping of global surface water and its long-term changes. *Nature*, 540, 418-422. https://doi.org/10.1038/nature20584.

Quenum, G.M.L.D., Arnault, J., Klutse, N.A.B., Zhang, Z., Kunstmann, H., Oguntunde, P.G. (2022). Potential of the Coupled WRF/WRF-Hydro Modeling System for Flood Forecasting in the Ouémé River (West Africa). *Water 2022*, 14, 1192. https://doi.org/10.3390/w14081192.

Rentschler, J., Salhab, M., Jafino, B. (2022). Flood exposure and poverty in 188 countries. *Nature Communications* 13.1, https://doi.org/10.1038/s41467-022-30727-4.

Rubel, O., Lukin, V., Rubel, A., Egiazarian, K., 2021. Selection of Lee Filter Window Size Based on Despeckling Efficiency Prediction for Sentinel SAR Images. *Remote Sensing* 13, 1887. https://doi.org/10.3390/rs13101887

Santos da Silva., S. Calmant, O. Rotuono Filho, F. Seyler, G. Cochonneau, E. Roux,

J. W. Mansour, Water Levels in the Amazon basin derived from the ERS-2 and ENVISAT Radar Altimetry Missions, *Remote Sensing of the Environment*, 2010, https://doi.org/10.1016/j.rse.2010.04.020

Sultan, B., Janicot, S. 2003. The west african moonsoon dynamics. Part II: the "preonset" and "onset" of the summer monsoon.

Tramblay, Y., Villarini, G., Zhang, W. (2020). Observed changes in flood hazard in Africa. *Environmental Research Letters* 15.10, https://doi.org/10.5194/essd-13-1547-2021.

United Nations International Strategy for Disaster Reduction (UNDRR) (2018).

Wang, L., Cui, S., Li, Y., Huang, H., Manandhar, B., Nitivattananon, V., Fang, X., Huang, W. (2022). A review of the flood management: from flood control to flood resilience. *Heliyon* 8.11, https://doi.org/10.1016/j.heliyon.2022.e11763.

Xie, Y., Zeng, H. Yang, K., Yuan, Q., Yang, C. (2023). Water-Body Detection in Sentinel-1 SAR Images with DK-CO Network. *Electronics* 12.14, https://doi.org/10.3390/electronics12143163.